Contents lists available at ScienceDirect

Transactions of Nonferrous Metals Society of China

36(2026) 796−817

www.tnmsc.cn

Processing, microstructure, and mechanical properties of additive manufacturing Inconel 625 using hot wire laser metal deposition

Guo-xing SU, Yu SHI *, Chun-kai LI, Guang LI, Gang ZHANG

State Key Laboratory of Advanced Processing and Recycling Non-ferrous Metals, Lanzhou University of Technology, Lanzhou 730050, China

Abstract: Inconel 625 alloy components were fabricated using hot wire laser metal deposition (HW-LMD) through process optimization, achieving a wire deposition rate of 1.72 kg/h. The microstructure and mechanical properties of the HW-LMD Inconel 625 alloys were systematically investigated. The results revealed that the microstructure of the HW-LMD Inconel 625 alloys consisted of columnar dendrites, characterized by an average grain size of 12.5 μm and a strong {100}⟨001⟩ texture. The main phase identified was γ-Ni, with the precipitation of Laves phase, measuring less than 1 μm, observed in the inter-columnar dendritic regions. The average microhardness of the HW-LMD Inconel 625 alloys was $HV_{1.0}$ 258. The yield strength and ultimate tensile strength were 493.5 and 837.4 MPa, respectively, with elongation exceeding 50%. Impact absorbing energies at 25 and −78 °C were 223.08 and 200.24 J, respectively. Both the tensile and impact fracture surfaces exhibited dimples, indicating a ductile fracture mechanism during the deformation process.
Keywords: laser metal deposition; hot wire; Inconel 625 alloy; microstructure; mechanical properties

1 Introduction

Inconel 625 alloy is highly regarded in the petrochemical and aerospace industries due to its exceptional properties, such as high-temperature strength, excellent ductility, and outstanding corrosion resistance [1−3]. However, challenges arise from its stable atomic structure and the presence of hard phases in the alloy, leading to reported difficulties like significant tool wear and increased manufacturing costs when fabricating Inconel 625 components through traditional subtractive methods [4].

Laser additive manufacturing (LAM) is a metal processing technique that employs a high-precision laser to melt feedstock material and deposit layers successively, resulting in the production of components [5]. LAM offers numerous advantages when compared to traditional manufacturing methods, including increased flexibility, minimized manufacturing time, and reduced material wastage [6−8]. Additionally, compared to other metal additive manufacturing (MAM) techniques including wire and arc additive manufacturing (WAAM) and electron beam additive manufacturing (EBAM), LAM possesses several benefits, such as precise control over energy input, minimal deformation of the substrate, and no need for a vacuum manufacturing environment [9,10]. Consequently, LAM has gained significant traction in recent years for the repair and fabrication of high-valued metal parts with intricate geometric designs, specifically in the aerospace and defense industries [11]. Nevertheless, there are still drawbacks associated with the application of LAM in the production of Inconel 625 alloy.

The deterioration of the alloy's mechanical

Corresponding author: *Yu SHI, Tel: +86-931-2976688, E-mail: shiyu@lut.edu.cn
https://doi.org/10.1016/S1003-6326(25)66998-6
Received 7 July 2024; accepted 26 April 2025

properties, caused by both element segregation and the precipitation of undesirable Laves phase, is one of the key issues that urgently needs to be addressed. SUI et al [12] emphasized that reducing the size of the Laves phases in LAM Ni-based alloys can effectively slow down the initiation and propagation of cracks during the deformation process under stress. WANG et al [13], and KONG and HUANG [14] have demonstrated that post-treatment processes are effective for eliminating the Laves phase and enhancing the mechanical properties of LAM Inconel 625 alloy. However, a study by HU et al [15] showed that solution treatment (ST) improved the tensile strength of the LAM Inconel 625 alloy while significantly reducing its toughness. Similarly, ZHANG et al [16] reported that the aging heat treatment (AT) process resulted in the formation of pores, while the ST process caused the precipitation of rod-like brittle phases in the laser cladding Inconel 625 coating, thereby promoting the occurrence of fracture. Furthermore, KIM et al [17] found that after hot isostatic pressing (HIP), the laser powder bed fusion (LPBF) Inconel 625 alloy exhibited lower elongation, lower high-cycle fatigue, and shorter life in low-stress conditions at 650 °C compared to the wrought alloy. The aforementioned studies demonstrated that although post-heat treatment processes can effectively enhance the strength of LAM Inconel 625 alloys, they introduce several challenges, including the prolonged delivery time, increased production costs, and potential embrittlement of the alloys.

Traditional LAM processes (such as SLM) generally exhibit relatively low productivity, with build rates ranging from 2 to 40 cm^3/h. This limitation is another significant factor that hinders the practical application of LAM technology in engineering, particularly for the efficient fabrication of large-sized nickel-based alloy components, such as turbine disks with diameters reaching up to 2200 mm, required for aerospace engines and gas turbines [18−20]. Typically, increasing laser power can enhance the deposition rate of feedstocks by facilitating the melting of more materials. Nevertheless, this operation also presents several unavoidable drawbacks, including elevated equipment costs associated with high power lasers and reduced accuracy in component formation. Furthermore, prolonged cyclic heating from high power lasers during multi-layer and multi-pass deposition processes not only exacerbates the heat accumulation and the interaction of diverse types of intricate stresses, leading to serious deformation and defects like liquation cracks within the components [21,22], but also intensifies elemental segregation and promotes the formation of brittle Laves phases in heat-sensitive materials such as Inconel 625 alloy, ultimately compromising the mechanical properties of the alloy [23].

Hot wire laser metal deposition technology (HW-LMD) represents an advanced MAM method that utilizes additional resistance heating to preheat the filler wire before it is introduced into the molten pool [24]. Compared to powder systems, the wire feeding system used in HW-LMD possesses advantages such as lower preparation costs for the wire feedstocks and 100% material utilization efficiency [25,26]. Compared to conventional cold wire laser metal deposition (CW-LMD), HW-LMD significantly enhances the wire deposition rate and energy efficiency due to the resistive heating of the filler wire, as demonstrated by NOWOTNY et al [27] and PAJUKOSKI et al [28]. Additionally, preheating the filler wire effectively compensates for the laser energy required to melt the wire, thereby reducing the laser power applied to the molten pool. As a result, issues such as workpiece deformation, defects like cracks, significant elemental segregation, and the formation of brittle phases, which are typically caused by the application of high power lasers, are expected to be avoided in HW-LMD components. In summary, the HW-LMD technique can establish a balance between high productivity and desirable performance in the additive manufacturing of Inconel 625 components.

In this work, by using the HW-LMD technique, an attempt was made to enhance the filler wire deposition rate in the LAM process, with the objective of minimizing the formation of Laves phase in as-deposited Inconel 625 components. The forming characteristics, microstructure, and mechanical properties of the HW-LMD Inconel 625 components were thoroughly investigated. The findings of this research will contribute to establishing a theoretical framework and providing engineering experience for the efficient additive manufacturing of the large-sized Inconel 625 components.

2 Experimental

2.1 Materials

The substrate utilized in this investigation was AISI 1045 carbon steel, with the diameter of the shaft being 60 mm and the plate sized at 300 mm (length) × 200 mm (width) × 20 mm (thickness). The deposition material was ERNiCrMo-3 filler wire from Special Metal Company (USA), with a diameter of 1.2 mm. The chemical compositions of both the substrate (AISI 1045 carbon steel) and the ERNiCrMo-3 filler wire can be found in Table 1. Before deposition, the substrate surface was polished using abrasive paper and subsequently cleaned with acetone to eliminate oxides and enhance the laser absorptivity.

2.2 Experimental principle and system

Figure 1 showed the experimental principle and set-up of HW-LMD in this study. The HW-LMD technique mainly involved wire preheating, melting, and consolidation of the molten pool. A supplementary preheating power supply, loaded between the substrate and the wire feeding nozzle, was applied to heating the wire before it came into contact with the laser. As the wire was fed in, the substrate surface and preheated filler wire were rapidly melted by the laser energy, resulting in the formation of a molten pool. As the laser beam and substrate moved relative to each other, a deposited track was formed once the molten pool solidified. The controlled repetition of deposition tracks produced the 3D components. As depicted in Figs. 1(a) and (b), both the bulks and the hollow

Table 1 Chemical compositions of AISI 1045 carbon steel and ERNiCrMo-3 filler wire (wt.%)

Specimen	C	Ni	Cr	Mo	Fe	Nb	Al	Ti	Cu	Mn	Si
ERNiCrMo-3	0.03	61.47	21.5	9.0	4.0	3.6	0.2	0.2	−	0.50	0.50
AISI 1045 steel	0.42−0.50	≤0.30	≤0.25	−	Bal.	−	−	−	≤0.25	0.50−0.80	0.17−0.37

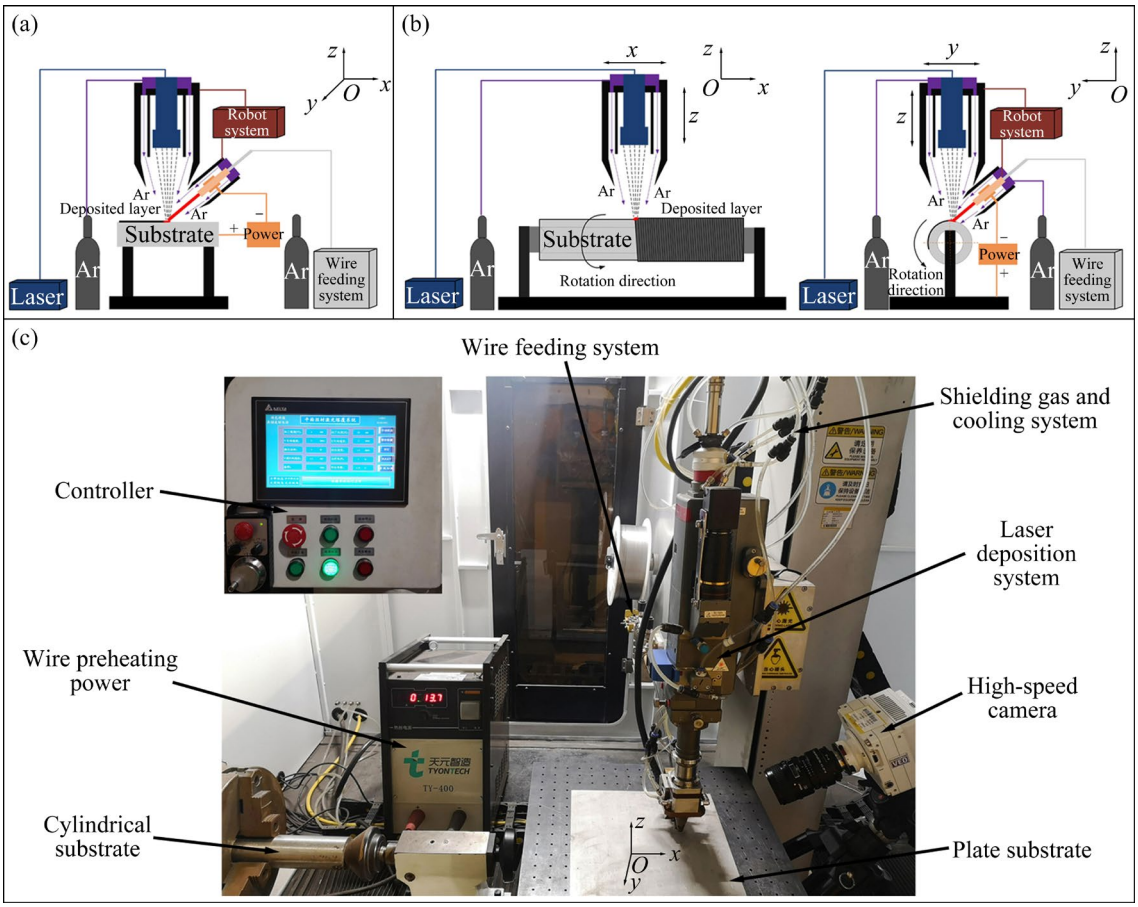

Fig. 1 Schematic diagrams of experimental principle and set-up: (a) Preparation principle of blocks; (b) Preparation principle of hollow cylindrical parts; (c) Experimental system

cylindrical parts could be integrally manufactured in this study.

Figure 1(c) illustrated the experimental setup mainly comprising a controller, a laser deposition system, a wire preheating and feeding mechanism, an Ar protection system, a four-axis linkage moving mechanism, a high-speed camera, and an infrared temperature acquisition system (not labeled in the figure). In this study, an IPG-4000 fiber laser with a maximum power of 4 kW was utilized. The diameter of the circular laser spot at the focal length was measured at 3 mm, with the focal plane consistently positioned on the surface of the substrate throughout the experiments. A wire feeder (JRS−400) was utilized to feed the filler wire into the melt bath at a fixed feeding angle of 45°. The preheating power source, a YC−400TX4 digital IGBT supplied by Panasonic, was employed to heat the filler wire before it contacted the molten pool, maintaining a constant output voltage of 5 V during the deposition process. To prevent the oxidation of the high-temperature molten pool and preheated wire, two streams of argon were used for shielding purposes. One stream, flowing at a rate of 20 L/min from the laser, shielded the welding pool, while the other stream, emanating from the wire feed nozzle, protected the filler wire. The four-axis linkage motion mechanism controlled the translational motion (x, y, and z directions) of the laser head and the rotation of the cylindrical substrate mounted on the flange chuck.

The molten pool image acquisition system comprised a high-speed camera (Phantom VEO710) and a high-pulse diode laser source. Equipped with a narrow band glass filter (having a central wavelength of 655 nm, bandwidth of 40 nm, and transparency of 85%), the high-speed video camera was employed to observe the wire preheating and transferring process in real time. Operating at an observation angle of 30° to the substrate surface, the camera captured images at a rate of 1000 frame/s. To ensure clear images of the deposition process, a high-pulse diode laser was used as supplementary lighting to illuminate the deposition zone. The laser emitted light at a wavelength of 810 nm, with a maximal pulse time of 10 μs, and a peak output power of 500 W. Additionally, a PYROLINE Uncooled IR Line camera (DIAS Infrared GmbH, Germany) was employed to monitor the preheating temperature of the filler wire. The camera operated at an internal measurement frequency of 512 Hz, providing a measurement accuracy of ±15 °C. The spectral range of the camera was from 1.4 to 1.8 μm, and its response time was 10 ms.

2.3 Research procedures

The research procedures in this study can be outlined as follows.

(1) The processes for fabricating Inconel 625 components were optimized, which involved optimizing the wire preheating process and determining the optimal single-track deposition process window. Subsequently, non-defective Inconel 625 components were produced using the optimized deposition conditions.

(2) To evaluate the production efficiency of the HW-LMD process, the wire deposition rate (m, in kg/h) and line energy (Q_L, in kJ/m) consumed during the deposition process were calculated through Eq. (1) [29] and Eq. (2) [30], respectively. Furthermore, the m and Q_L of HW-LMD technology were compared with other MAM technologies:

$$m=\rho v=\rho\frac{\pi D^2}{4}V_f \tag{1}$$

$$Q_L=\frac{P_L+UI}{V_S} \tag{2}$$

where ρ represents the density of the filler wire, which is 8.4×10^3 kg/m^3. The diameter of the filler wire, denoted as D, is 1.2 mm. The preheating voltage, represented by U, is maintained at a constant value of 5 V. Additionally, deposition process parameters P_L is the laser power, V_S is the laser scanning speed, V_f is the wire feeding speed and I correspond to the wire preheating current.

(3) The microstructure and phase composition of the HW-LMD Inconel 625 specimens were studied in detail. A comparison was performed on the mechanical performance of Inconel 625 specimens fabricated through HW-LMD and other manufacturing techniques. Insights into the interconnections among the deposition process, microstructural characteristics, and properties of the specimens were unveiled.

2.4 Observation and detection

After deposition, the surface roughness of the as-deposited components was examined using the confocal laser scanning microscope (LSM−800). The components were then sectioned into blocks

measuring 10 mm × 10 mm × 5 mm. These blocks were polished to 4000 grit and subsequently etched with aqua regia via an electrolytic process (6 V, DC, 5 s) at room temperature. Following this preparation, the microstructures of the as-deposited specimens were investigated using optical microscope (OM, Zeiss Axio Scope A1), scanning electron microscope (SEM, QUANTA FEG−450), and transmission electron microscope (TEM, JEOL JEM−2100F). To characterize the micro-texture and grain size distribution of the deposited specimens, electron backscattered diffraction (EBSD) test was conducted. Furthermore, X-ray diffraction (XRD) and energy dispersive spectroscopy (EDS) were employed to analyze the element composition and phase distribution of the deposited specimens, respectively, aiming to establish correlations between microstructure and mechanical performance.

To estimate the mechanical properties of Inconel 625 specimens produced by the HW-LMD method, various tests were performed. According to the ASTM E384—08 standard, the microhardness of the as-deposited specimens was assessed utilizing an HDX−1000 digital Vickers microhardness tester under a load of 1 kg (equivalent to 9.807 N), with a dwell time of 15 s and an indent spacing of 0.5 mm. Employing a Zwick/Roell Z100 tester, tensile tests were performed at a strain rate of 2.0 mm/min to characterize the tensile properties of HW-LMD Inconel 625 specimens. The dimensions of the tensile specimens were specified in Fig. 2(a) following ASTM E8/E8M — 21 standard recommendations. The V-shaped notch impact tests were conducted at ambient temperature (25 °C) and −78 °C. The impact absorbed energies were determined by averaging the results of three tests. The dimensions of the impact specimens adhered to the specifications detailed in the ASTM E23 — 2023 standard, as presented in Fig. 2(b). The surface morphologies of the tensile fractures and impact fractures were observed using SEM.

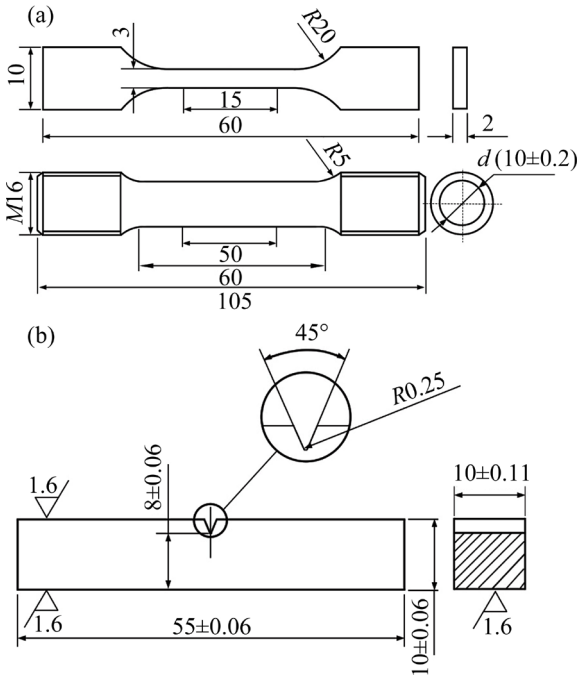

Fig. 2 Specimen dimensions for mechanical performance testing: (a) Tensile specimens; (b) Impact specimens (Unit: mm)

3 Results and discussion

3.1 Preparation process

3.1.1 Optimization of wire preheating process

To achieve better performance of HW-LMD Inconel 625 components, it is essential to increase the proportion of resistive heating in the total heat input for melting the filler wire, while maintaining deposition stability. Based on the research conducted by WEI et al [31] and HUANG et al [32], the temperature distribution function along the length of the ERNiCrMo-3 filler wire can be defined by

$$(\alpha-\beta)\ln(1+\alpha T)+\alpha\beta T=\frac{16\lambda_0\alpha^2 I^2}{C_0 V_f \rho\pi^2 D^4}x+25\alpha\beta \tag{3}$$

where α is a coefficient, approximately 2.5×10^{-4} °C^{-1}; β is a constant coefficient set as 6.0×10^{-4} °C^{-1}; T represents the temperature of the filler wire at a distance x (in mm) from the wire feeding nozzle, in °C; C_0 stands for the specific heat capacity of the filler wire at room temperature (25 °C), being 410 J/(kg·°C); λ_0 is the resistivity of the filler wire at room temperature, being 1.28×10^{-6} Ω·m.

The aforementioned mathematical model for wire preheating was utilized to calculate the wire tip temperature for a wire feeding rate of 3 m/min, considering varied wire preheating currents. The theoretical calculation indicated that the temperature at the wire end could reach 823 °C with a preheating current of 110 A. Correspondingly, temperatures of 1123 and 1459 °C were calculated at preheating currents of 120 and 140 A, respectively. Correspondingly, Figs. 3(a1−a3) presented the practical temperature distribution of the filler wire as

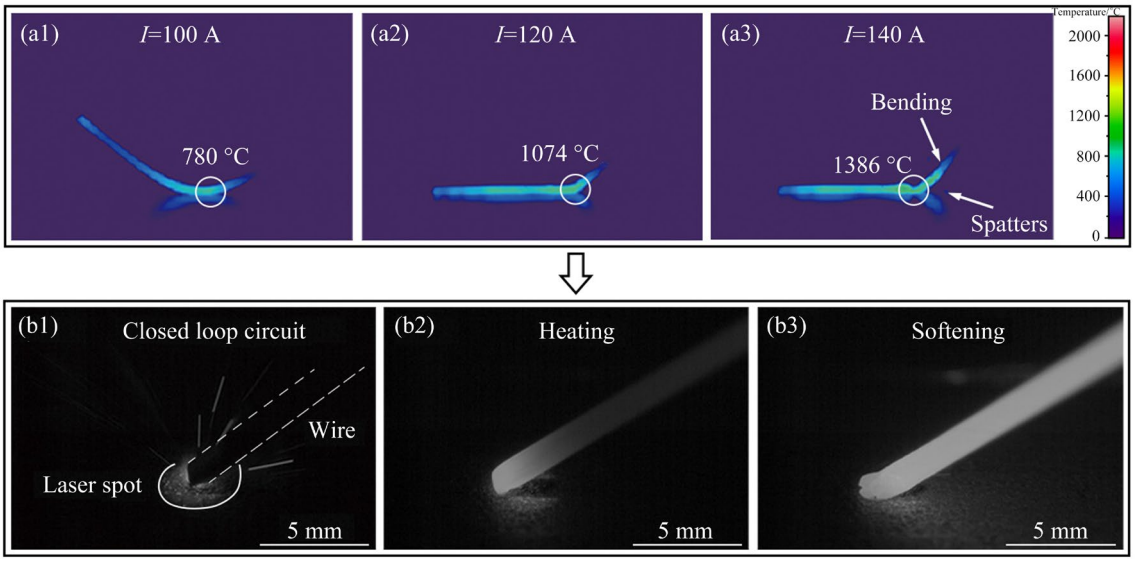

Fig. 3 Optimization of wire preheating process: (a1−a3) Temperature field distribution of filler wire with varied preheating currents at wire feeding speed of 3 m/min; (b1−b3) Optimized wire preheating process captured by high-speed camera

captured by an infrared camera. Due to radiative heat dissipation, the actual preheating temperature of the wire tip was slightly lower than the theoretically calculated value. However, the deviation remained within an acceptable range, indicating that the theoretical calculation model is effective. In Fig. 3(a1), when the preheating current was 100 A, inadequate preheating of the filler wire led to an undesirable situation where a stable deposition process required higher laser energy. With an increase in the preheating current, the temperature of the filler wire increased. As depicted in Fig. 3(a2), when the preheating current of the filler wire reached 120 A, the temperature of the wire tip was close to its melting point, indicating a good preheating state. When the preheating current reached 140 A, the temperature at the wire tip exceeded its melting point. As illustrated in Fig. 3(a3), the filler wire was entirely melted under the effect of resistance heating, resulting in the formation of spatters. At the same time, the wire was softened severely, and the wire's directional stability was deteriorated, indicating that a stable deposition process was difficult to obtain. According to the aforementioned analysis, it could be inferred that a preheating current of approximately 120 A is suitable for a wire feeding rate of 3 m/min. Considering the additional heating effect generated by the laser energy during the actual deposition process, a preheating current of 110 A is considered to be a preferable choice.

Figures 3(b1−b3) depicted the wire preheating process at the optimized preheating current of 110 A. At the beginning of the wire preheating process, as depicted in Fig. 3(b1), the wire tip contacted the substrate surface, creating a closed circuit of preheating current. As the preheating process progressed, Fig. 3(b2) illustrated that the wire was heated up sufficiently by the resistant heat, increasing its temperature. At the end of the preheating process, as shown in Fig. 3(b3), the wire tip was softened, accompanied by good wire pointing stability.

3.1.2 Optimization of single-track deposition process

In Figs. 4(a1−a3), the HW-LMD process for preparing single deposited track was optimized, focusing on two key variables: laser power P_L and laser scanning speed V_S. Figure 4(a1) showed that relatively low laser power and high laser scanning rate resulted in insufficient energy per unit length of the track. Hence, the wire was not sufficiently melted, leading to unsatisfactory deposition track performance. It was determined that a laser power greater than 1750 W and a laser scanning speed less than 3 m/min were necessary for a consistent and stable deposition process. In Fig. 4(a2), the laser power was increased to 2000 W, resulting in a significantly optimized formation of the deposition layer compared to Fig. 4(a1). However, some undercuts were still observed, which were attributed to inadequate spreading of the molten pool. With further increase in laser power and the decrease in laser scanning speed, as presented in Fig. 4(a3), the

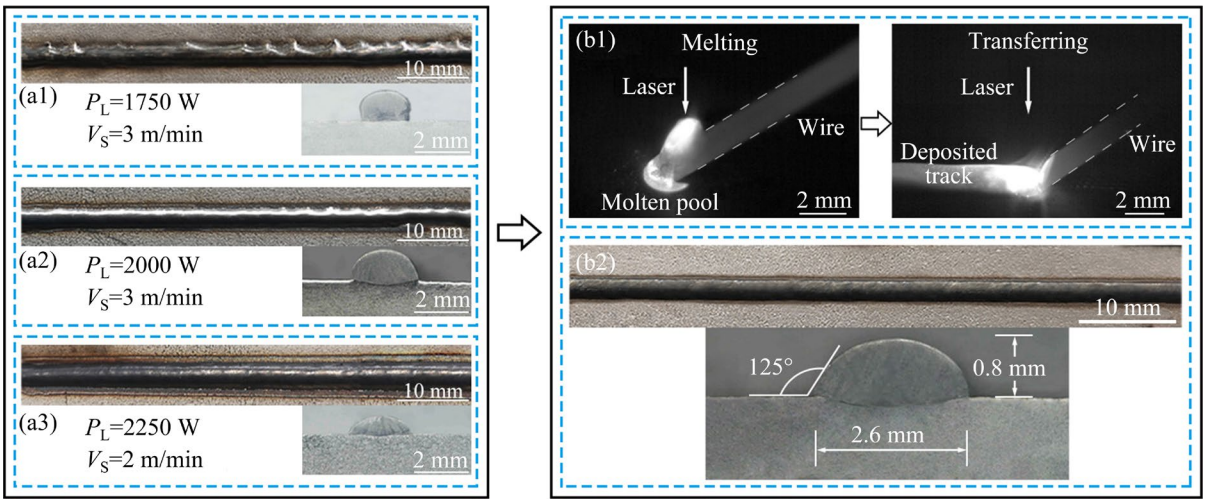

Fig. 4 Schematic diagrams showing preparation process of optimal single deposited track: (a1−a3) Optimization of process parameters; (b1, b2) Deposition process and macro-morphology of optimal deposition track, respectively

filler wire was sufficiently melted, resulting in a smooth and flat single-track without the formation of undercuts. Nevertheless, the increased power density led to a deposited track with a small aspect ratio and deep penetration, which was not conducive to an efficient additive process. Therefore, laser power less than 2250 W and laser traverse speed greater than 2 m/min were considered suitable for achieving favorable deposition. Based on the above analysis, parameter combinations within the intervals from 2000 to 2250 W for laser power and from 2 to 2.5 m/min for laser scanning rate were expected to ensure a consistent deposition process and favorable deposited tracks.

Figures 4(b1, b2) displayed the wire transfer process and the morphology of the deposition track obtained at an optimized combination of process parameters, including a laser power of 2000 W, a laser scanning rate of 2.5 m/min, a wire feed rate of 3 m/min, a wire preheating current of 110 A, and front wire feeding mode with the wire tip positioned at the rear of the welding pool. As shown in Fig. 4(b1), after being preheated by resistance heating, the wire tip was fully melted under the irradiation of a portion of laser energy. At the same time, the remaining laser energy irradiated the substrate to form a shallow molten bath. Additionally, a steady liquid bridge was established between the welding pool and the wire tip. Subsequently, as the laser beam and substrate moved relative to each other, the molten pool solidified, leading to the formation of a deposited track. As depicted in Fig. 4(b2), the optimal single Inconel 625 track had a width of 2.6 mm, a height of 0.8 mm, and a deposition angle of 125°. The surface of the deposited track was uniformly smooth, without any visible defects. Furthermore, the cross-sectional view of the track was symmetrical and exhibited a good bond with the substrate.

3.1.3 Preparation of multi-layer and multi-pass deposited components

Based on the deposition strategies shown in Fig. 5(a), the Inconel 625 components were successfully manufactured through sequentially accumulating the optimal single deposited tracks, maintaining a spacing of 1.25 mm between adjacent tracks. Figure 5(b) illustrated the typical wire transfer process observed during the multi-layer and multi-track deposition process. It can be observed from the figure that the filler wire consistently came into contact with the molten bath, creating a continuous closed loop of preheating current. This ensured effective heating of the filler wire, leading to its complete melting and smooth transfer into the molten pool through a steady liquid bridge. The resulting Inconel 625 components were presented in Fig. 5(c). The bulk part had approximate dimensions of 150 mm × 50 mm × 20 mm, and a cylindrical component measuring 200 mm in length and 15 mm in thickness was also achieved. The as-deposited components exhibited smooth surfaces without any visible defects or deformations.

The surface profile of the as-deposited components was measured using a color three-dimensional laser microscopic system, as displayed in Fig. 6(a). The results revealed that the maximum

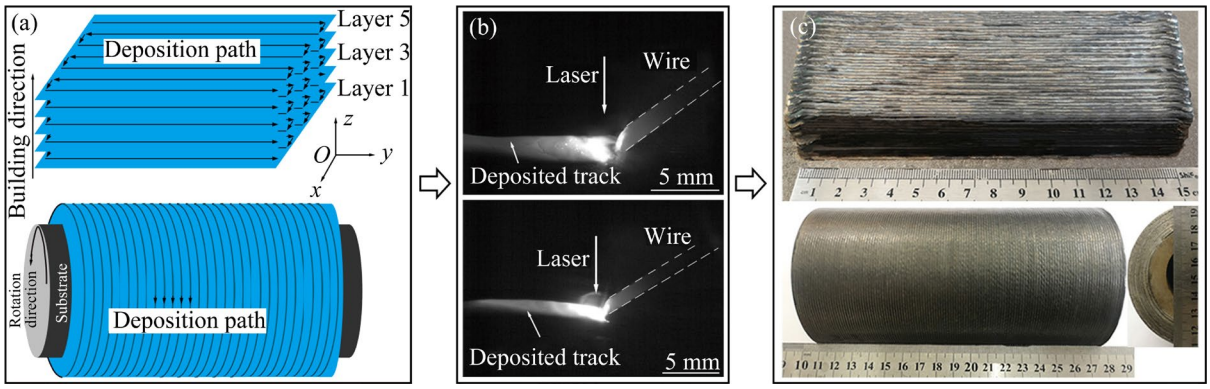

Fig. 5 Forming process and appearance of HW-LMD Inconel 625 components: (a) Deposition paths; (b) Wire transfer processes; (c) Appearance of HW-LMD Inconel 625 components

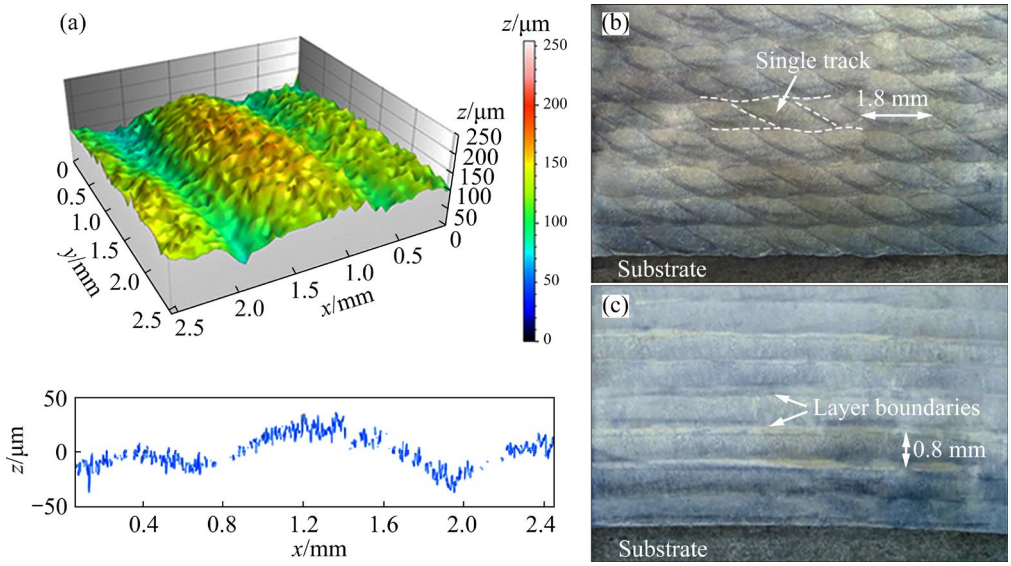

Fig. 6 Macro-morphologies of HW-LMD Inconel 625 components: (a) Surface appearance; (b) Transverse section; (c) Longitudinal section

height difference of the surface was approximately 75 μm, and the average surface roughness (R_a) of the components was measured to be 5.73 μm. The macro-morphologies of the transverse and longitudinal sections of the HW-LMD Inconel 625 components were presented in Figs. 6(b, c), respectively. It revealed that the width of each deposited track was approximately 1.8 mm, with an interlayer thickness of around 0.8 mm. The boundaries between the deposited layers were nearly parallel, demonstrating a strong metallurgical bond.

3.2 Deposition rate and line energy

Substituting the optimized process parameters into Eq. (1) and Eq. (2), the wire deposition rate was found to be 1.72 kg/h and the line energy was determined to be 61.3 kJ/m, respectively. After reviewing the research results of other researchers in Refs. [33−41], the feedstock deposition rate and line energy of different AM processes for fabricating Inconel 625 alloy were summarized in Fig. 7. Figure 7 demonstrated that the HW-LMD technique employed in this investigation achieved a significantly higher feedstock deposition rate compared to the conventional SLM process while maintaining similar energy consumption [33−35]. Moreover, when compared to traditional LMD technology, the HW-LMD technique consumed much less energy for depositing the same volume of feedstocks [9,33,36,37]. Additionally, compared to the WAAM, the wire deposition rate for HW-LMD was around twice as high as that of TIG-WAAM (0.688 kg/h) and reached nearly 50% that of CMT-WAAM (3.725 kg/h) and 30% that of MIG-WAAM

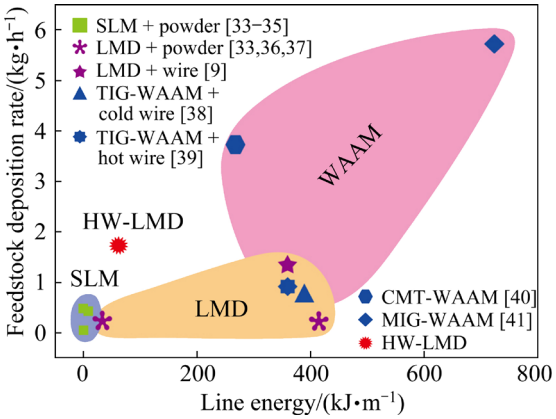

Fig. 7 Comparison of feedstock deposition rate and line energy of various additive manufacturing processes for preparing Inconel 625 alloy

(5.73 kg/h). However, the line energy applied in the HW-LMD process was only 15.7% that of TIG-WAAM, 22.7% that of CMT-WAAM, and 8.5% that of MIG-WAAM, respectively [38−41]. These results demonstrated that the HW-LMD process exhibited superior energy efficiency compared to other MAM methods.

3.3 Microstructure and phase composition

3.3.1 Microstructure

The microstructures of the HW-LMD Inconel 625 specimens were presented in Fig. 8. Figure 8(a) provided a comprehensive three-dimensional optical view, encompassing the transverse section (*x*-*O*-*z*), the lengthwise section (*y*-*O*-*z*), and the horizontal section (*x*-*O*-*y*). Magnified images of specific zones indicated in Fig. 8(a) were depicted in Figs. 8(b−f) for further investigation.

It has been noted that the final microstructure morphology of the as-deposited alloy was closely correlated with the ratio of the temperature gradient (G) to the cooling rate of the molten pool (R) [42]. Previous analyses demonstrated that the HW-LMD technique employed in this study exhibited a higher wire deposited rate and lower line energy. Consequently, there was a notable decrease in the heat applied to the molten pool, leading to lower temperature gradients and higher cooling rates within the molten pool. Thus, as seen in Fig. 8(a), the HW-LMD Inconel 625 alloy primarily consisted of columnar dendrites. The growth direction of these columnar dendrites was determined by the direction opposite to the heat flux during laser deposition. As evident from Fig. 8, the substrate or the previously solidified deposited layer served as the heat dissipater during the molten pool solidification process, and most of the heat vertically transferred from the molten bath into the substrate, partly through the adjacent solidified deposited track [43]. Consequently, a downward heat flux direction was

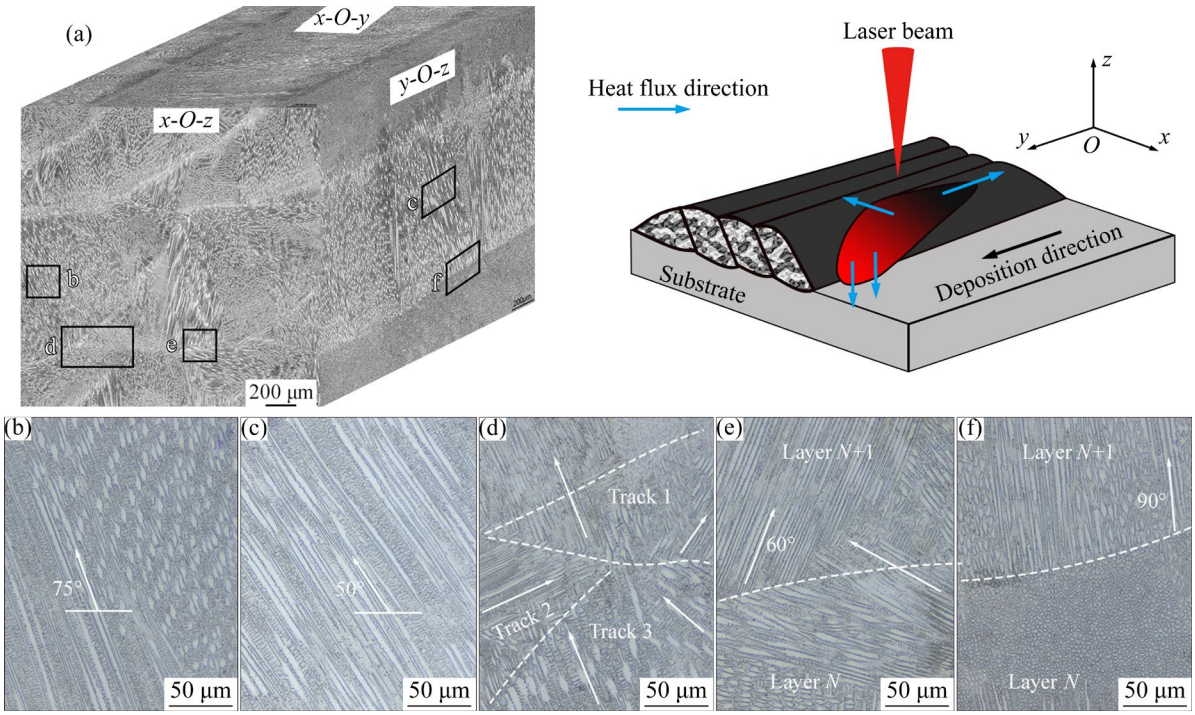

Fig. 8 Microstructures of HW-LMD Inconel 625 alloy: (a) Three-dimensional optical view; (b−f) Magnified images of specific zones

established at an angle ranging between 50° and 75° relative to the substrate surface. Accordingly, as depicted in Figs. 8(b, c), typical epitaxial columnar structures with angles exceeding 50° but less than 75° were observed in the bottom or middle region of each deposited layer.

In the upper region of the molten pool, the orientation of the temperature gradient changed due to the combined effects of contacting with air and previously solidified tracks. Most of the heat in the top region of the molten pool was transferred to the adjacent solidified track rather than to the substrate. As a result, a portion of columnar dendrites grew from the trailing end of the molten pool. This resulted in an evolution of the grain morphology, with vertical columnar dendrites (in the z direction) transitioning to horizontal columnar dendrites (in the x direction). The horizontal columnar dendrites developed almost parallel to the substrate in the transverse section (x-O-z) (refer to Fig. 8(e)), while displaying typically isometric structures in the longitudinal section (y-O-z) (refer to Fig. 8(f)). The observation in this particular region aligned with the findings of laser cladding Inconel 625 reported by ABIOYE et al [44].

As shown in Fig. 8(d), the microstructural features in the overlapping zone of the HW-LMD Inconel 625 specimens were more intricate compared to the non-overlapping zone. This intricacy can be attributed to the complex direction of heat dissipation. The overlapping zone mainly comprised coarse columnar dendrites with random orientations (see white arrows). Figures 8(e, f) presented the micromorphologies at the boundaries between successive deposited layers. Due to the remelting effect of the subsequent deposited layer on the top area of the already solidified deposited layer, the previously formed grain crystals served as the pre-nuclei for the formation of forthcoming columnar crystals during the re-solidification, i.e. epitaxial solidification. Therefore, following the findings of WANG et al [45], epitaxial columnar dendrites at the boundaries extended from the boundaries towards the center of the deposited layer or expanded directly through the boundaries.

To observe the crystallographic texture and grain size distribution in HW-LMD Inconel 625 specimens, EBSD analyses were conducted in a 2 mm × 2 mm region of the cross-section (x-O-z). The results were depicted in Fig. 9. As illustrated in Fig. 9(a), typical columnar structures were observed in the HW-LMD Inconel 625 specimens. The pole figure (PF) and inverse pole figure (IPF) presented in Fig. 9(b) revealed a strong texture of {100}⟨001⟩, aligning with the prior analysis using the optical microscope. Furthermore, due to the relatively low energy input applied to the feedstock on a per-unit volume in this study, the molten pool solidified quickly along with a sharp decrease in molten pool temperature. Consequently, the HW-LMD Inconel 625 specimens exhibited an average grain size of 12.5 μm, with most grains measuring below 10 μm, and a few grains measuring over 50 μm, as shown in Fig. 9(c).

The microstructure of the HW-LMD Inconel 625 specimens was further examined by SEM. As shown in Figs. 10(a, b), low-magnification SEM images of the transverse and longitudinal sections clearly showed the boundaries between the deposited tracks and layers, with no discernible microscopic defects such as cracks, pores, or incomplete fusion identified within the specimens. In the higher-

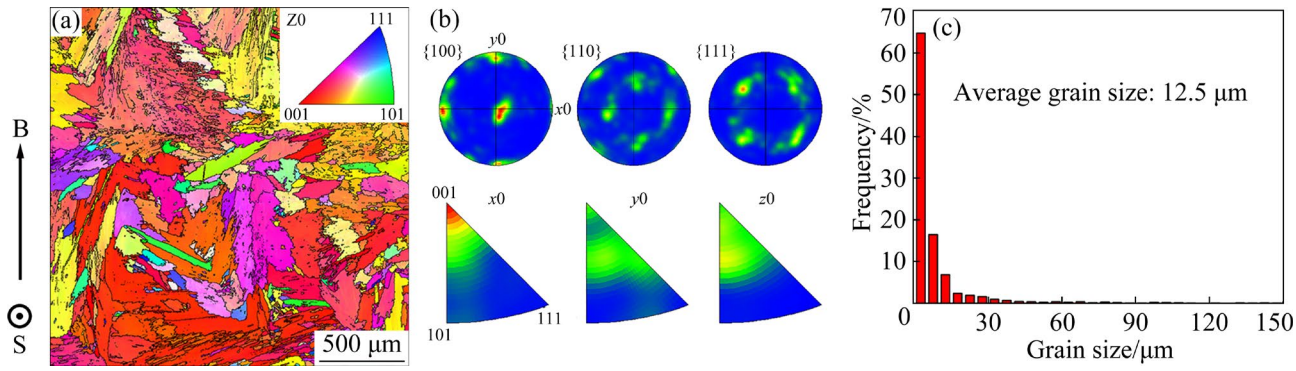

Fig. 9 EBSD analysis results of HW-LMD Inconel 625 specimens: (a) EBSD map; (b) PF and IPF maps; (c) Distribution of grain size (B represents the building direction and S stands for the deposition direction)

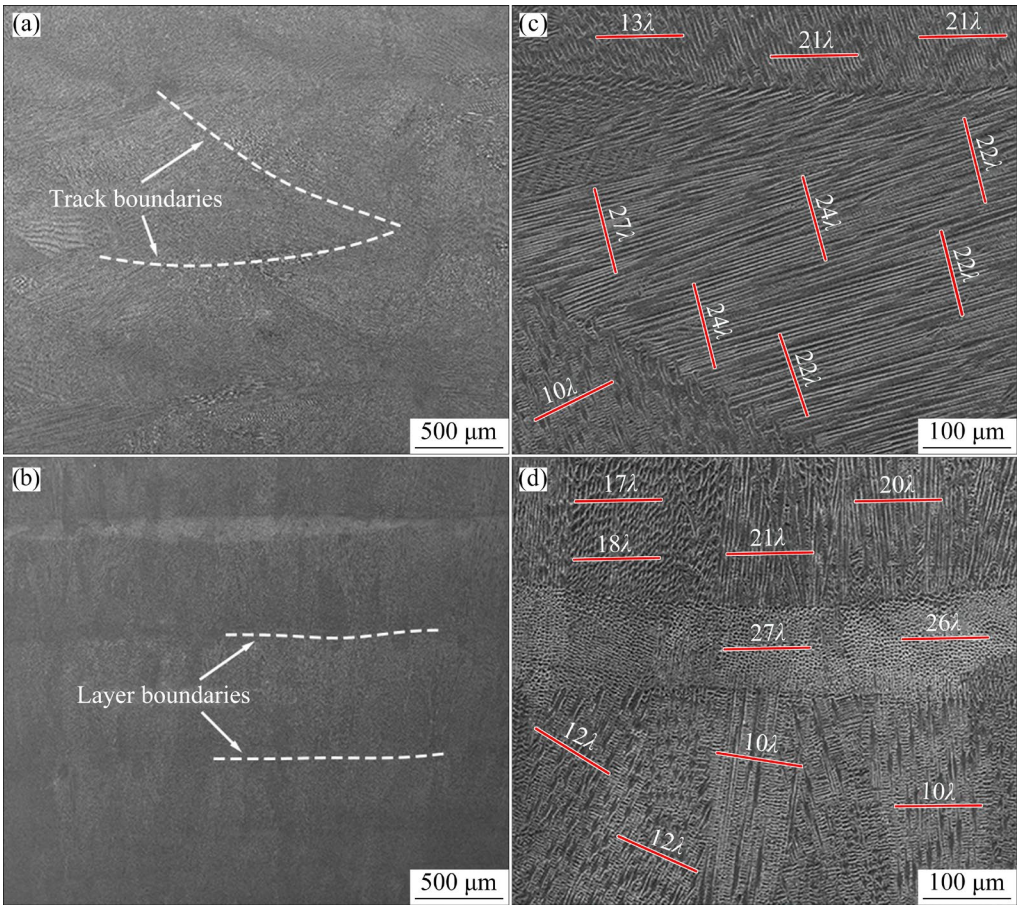

Fig. 10 SEM images of HW-LMD Inconel 625 specimens: (a, c) Transverse section; (b, d) Longitudinal section ((c, d) For measurement of PDAS (λ))

magnification SEM images depicted in Figs. 10(c, d), columnar dendrites were observed growing perpendicularly to the boundaries of the deposited tracks and layers, consistent with the results of the previous OM and EBSD analyses. Based on Figs. 10(c, d), the average primary dendrite arm spacing (PDAS) was determined utilizing the linear intercept method outlined in Eq. (4) [46]:

$$\overline{\lambda} = \frac{N \cdot L}{n} \tag{4}$$

where $\overline{\lambda}$ represents the average PDAS, N denotes the total number of red lines (N=20) in Figs. 10(c, d), L represents the length (L=100 μm) of a single line perpendicular to the primary dendrite arm, and n represents the total number of primary dendrites crossed by the lines (n=379). By applying Eq. (4), the average PDAS was determined to be approximately 5.28 μm. It is worth noting that the PDAS is closely associated with the cooling rate ($\dot{T}$, in K/s) of the molten pool. According to Eq. (5) [47], the cooling rate $\dot{T}$ of the molten pool during the HW-LMD process was calculated to be around 8.61×10^4 K/s.

$$\overline{\lambda} = 80\dot{T}^{-0.3} \tag{5}$$

3.3.2 Phase composition

In Fig. 11(a), small-sized precipitates were found in the inter-dendrite regions, suggesting the possible presence of secondary phases. Initially, the phase composition of the HW-LMD Inconel 625 specimens was determined using XRD. The results in Fig. 11(b) revealed that the main diffraction peaks were found at 2θ values of 43.5°, 50.7°, 74.6°, and 90.5°, corresponding to the preferred crystal planes of (111), (200), (220), and (311), respectively. This indicated that γ-Ni was the predominant phase present in the HW-LMD Inconel 625 specimens [48]. It should be noted that identifying secondary precipitates via the conventional SEM and XRD methods may be challenging due to their small size.

Hence, the potential secondary phases in the inter-dendritic regions were further examined via TEM. In the bright-field (BF) TEM images depicted

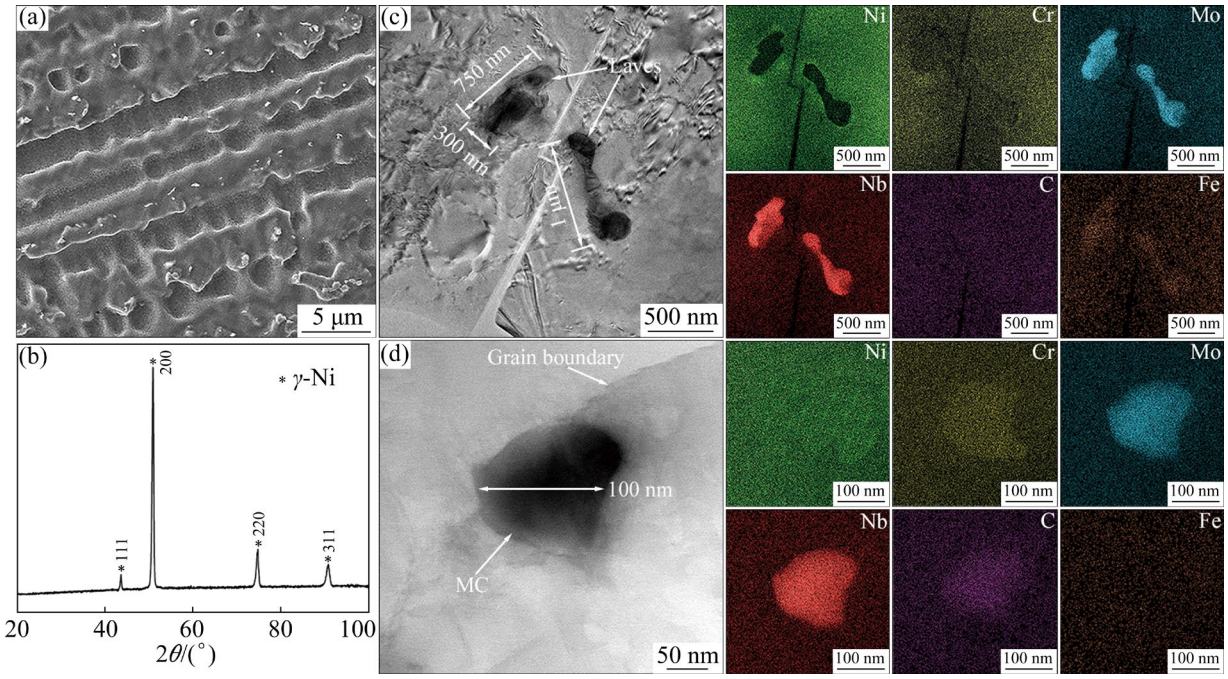

Fig. 11 Analysis results of precipitates in inter-dendritic regions: (a) SEM image; (b) XRD pattern; (c, d) BF-TEM images

in Fig. 11(c), diffusely distributed rod-shaped secondary phases with sizes smaller than 1 μm were observed in the inter-dendritic regions. The corresponding EDS analysis results indicated higher contents of elements including Nb and Mo, but a lack of Ni and Cr in comparison to the matrix phase. Based on a pertinent study conducted by LUO et al [49] on DED Inconel 718/Haynes 25 functionally graded material, these irregularly shaped precipitates were identified as Laves phase. Contrastingly, the BF-TEM image in Fig. 11(d) demonstrated the presence of spherical precipitates situated at the grain boundaries, measuring approximately 100 nm. The elements' composition indicated that these spherical particles exhibited notably higher contents of Mo, Nb, Cr, and C in comparison to the matrix. The spherical nano-precipitates observed at the grain boundaries were hypothesized to be carbides, such as Nb-rich MC, Mo-rich M_6C, or $M_{23}C_6$, which aligned with the findings reported by KELLER et al [50].

Figure 12 illustrated the precipitation process of secondary phases during the solidification of Inconel 625 alloy. Typically, the solidification of Inconel 625 was initiated at 1380 °C. Meanwhile, due to the low equilibrium distribution coefficients of high atomic mass metallurgical elements like Nb (0.271) and Mo (0.766) [51], they inevitably migrated from the solid phase to the liquid phase (Fig. 12(a)). Then, as shown in Fig. 12(b), a layer enriched with Nb or Mo was formed at the solid−liquid interface, and the thickness of which was related to the solidification rate of the molten pool. As the solidification process progressed, primary dendrites of columnar crystals grew epitaxially, with the formation of secondary dendritic arms. Consequently, the Nb/Mo-enriched layers were divided into several smaller fragments. As the temperature of the molten pool rapidly decreased, the eutectic reaction $L = \gamma + \text{NbC}$ occurred at 1295 °C, resulting in the formation of the eutectic compound γ/NbC, which depleted most of the Nb in the liquid. Subsequently, the eutectic reaction $L = \gamma + \text{Laves}$ occurred at 1150.8 °C, depleting the remaining elements and resulting in the formation of a small quantity of γ/Laves. This signified the termination of the solidification process. Therefore, as seen in Fig. 12(c), the eutectic compounds of γ/NbC and γ/Laves were typically the major secondary phases detectable in the inter-dendritic regions of Inconel 625 alloy.

The formation of secondary phases in the LAM Inconel 625 alloy was predominantly governed by the contents of elements such as Mo and Nb in the liquid and the cooling rate of the molten pool. In this study, the molten pool solidified with a cooling rate of 8.61×10^4 K/s due to the relatively low line energy.

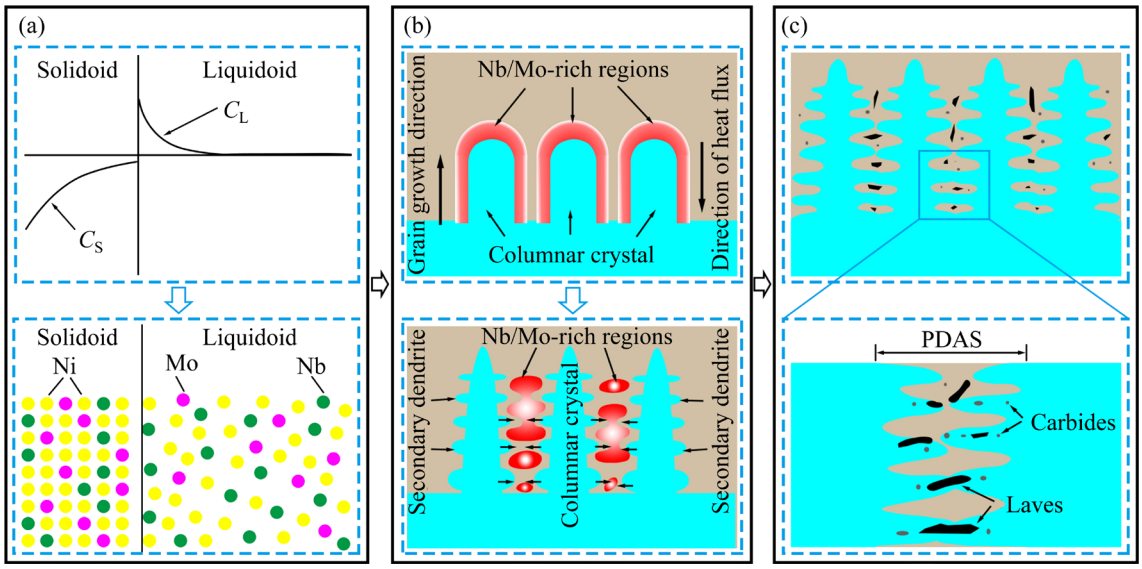

Fig. 12 Schematic diagrams of formation of precipitates in inter-dendritic regions: (a) Element diffusion; (b) Formation of Nb/Mo-rich regions; (c) Precipitation of secondary phases

Although this cooling rate is lower than that of traditional powder bed fusion (PBF) technology (10^5−10^7 K/s) [52], it is significantly higher than that of conventional DED technology (10^3−10^5 K/s) [53]. Consequently, the limited time for solute redistribution during the HW-LMD process significantly increased the alloying elements' solubility within the γ-Ni matrix, reducing elemental segregation in the inter-dendritic regions and inhibiting the formation of large-sized secondary phases. Moreover, the higher cooling rate of the molten pool led to a smaller grain size of columnar dendrites, accompanied by finer secondary dendrites. This resulted in more, but smaller and better-separated inter-dendritic regions. Thus, the size of the secondary phases in the intergranular regions was limited by the PDAS [54]. Overall, in the intergranular regions of HW-LMD Inconel 625 specimens, only nano-scale metallic carbides and a small quantity of Laves phase were observed.

3.4 Mechanical properties

3.4.1 Microhardness

The microhardness distribution of the HW-LMD Inconel 625 specimens was tested from the uppermost layer to the lowest layer, with the results presented in Fig. 13(a). The findings indicated that the hardness of the HW-LMD Inconel 625 specimens uniformly ranged between $HV_{1.0}$ 250 and $HV_{1.0}$ 265 throughout the layers, with no significant softening zone observed. The average hardness value was

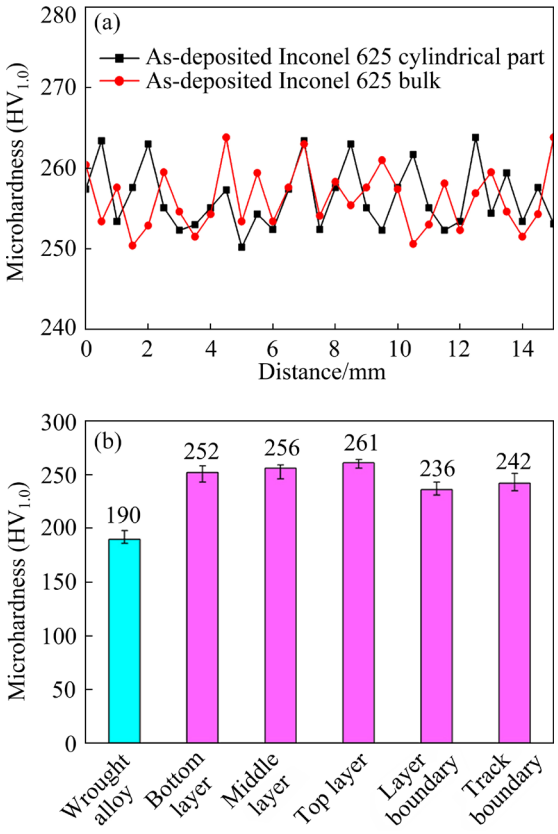

Fig. 13 Microhardness of HW-LMD Inconel 625 specimens: (a) Microhardness distribution from uppermost layer to lowest layer; (b) Microhardness for different characteristic zones

approximately $HV_{1.0}$ 258, reflecting a 35.7% increase compared to the microhardness of the wrought Inconel 625 alloy, which was measured at $HV_{1.0}$ 190. To accurately analyze microhardness

variations of the HW-LMD specimens, repetitive testing was conducted in different regions. Notably, as illustrated in Fig. 13(b), the microhardness of the lower layer was slightly lower than that of the top layers. The reduced microhardness in the lower layers can be attributed to the thermal cycle caused by the subsequent deposition layer, resulting in the formation of coarse columnar dendrites with larger secondary dendritic arm spacings. It is well-established that coarse grains typically result in reduced hardness [55]. Additionally, the hardness at the boundaries between adjacent deposited tracks or layers was lower than that in other regions, likely due to the presence of coarsened grains with random growth directions, a phenomenon previously discussed.

3.4.2 Tensile properties

Figure 14 depicted the locations where mechanical property testing specimens were machined. Tensile tests of the as-deposited bulk were conducted using sheet-shaped specimens, as depicted in Fig. 14(a), with the applied tensile load in the same direction as the deposition direction. For the as-deposited cylindrical part, rod-shaped tensile specimens were utilized, as presented in Fig. 14(b), with the applied tensile load perpendicular to the deposition direction.

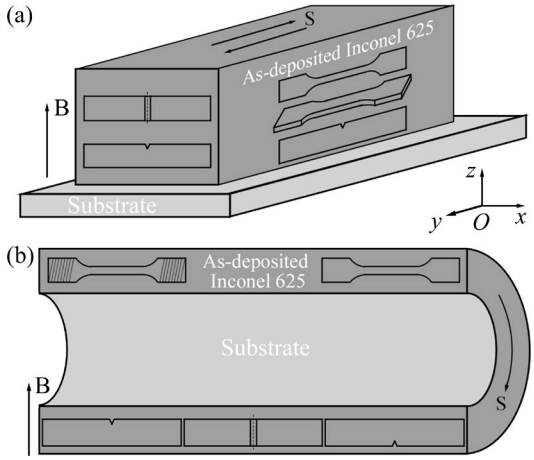

Fig. 14 Specimen machining positions for mechanical properties testing: (a) In as-deposited bulk; (b) In as-deposited cylindrical part (B denotes the building direction and S represents the deposition direction)

The results from the tensile tests, conducted three times for all specimens, are presented in Table 2 [35,38,40,41,56−58], with the corresponding stress−strain curves depicted in Fig. 15. The average ultimate tensile strength (σ_b) of the HW-LMD Inconel

Table 2 Comparison of tensile performance for Inconel 625 alloy produced by different manufacturing methods

Method and material	Microstructure characteristic	Ultimate tensile strength, σ_b/MPa	Yield strength, $\sigma_{0.2}$/MPa	Elongation/ %
HW-LMD specimens (*y* direction)	Columnar dendrites with average grain size of 12.5 μm; PDAS: 5.28 μm; Laves phase size: 1 μm	828.7−846.3	484.3−504	52.4−57.4
HW-LMD specimens (*x* direction)		817.4−829.8	478.2−492.5	49.8−54.3
Wrought alloy	−	875.37	521.29	57.12
Casting alloy [56]	−	710	350	48
Binder jetting + powder [57]	Average grain diameter: 57 μm, having porosity	707	320	58.74
LMD + powder [57]	Fine cellular/dendrites; secondary phase: Nb-rich MC and Cr-rich $M_{23}C_6$	1000	656	24
SLM + powder [35]	Columnar dendrites; primary dendritic spacing: 0.96 μm	878.5	641.5	30
EBAM + powder [58]	Columnar grain width: 20−500 μm; equiaxed grain size: 15 μm	750	410	44
CMT-WAAM [40]	Cellular dendrites with dendritic spacing of 30−40 μm	647.9	376.9	46.5
TIG-WAAM [38]	Columnar dendrites; PDAS: 13−35 μm; Laves phase size: 5 μm	684	−	40.13
MIG-WAAM [41]	Columnar dendrites; secondary phase: NbC and Laves	696.5	335	46.68

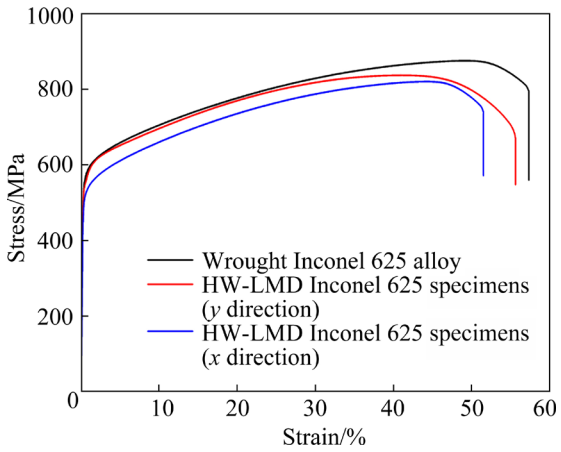

Fig. 15 Stress−strain curves of different specimens in tensile properties test

625 alloy along the deposition direction was 837.4 MPa, with an average yield strength ($\sigma_{0.2}$) of 493.5 MPa, while perpendicular to the deposition direction, the values were 822.6 and 486.7 MPa, respectively. In comparison, for the wrought Inconel 625 alloy, σ_b was 875.37 MPa, and $\sigma_{0.2}$ was 521.29 MPa. The tensile strength of HW-LMD Inconel 625 specimens was slightly higher in the deposition direction compared to specimens machined perpendicularly to the deposition direction. Table 2 also summarized the tensile performance of Inconel 625 alloy produced using various manufacturing techniques. In comparison, the tensile properties of the HW-LMD specimens were slightly inferior to those of specimens produced through traditional LAM methods such as SLM and powder-based LMD, but they reached approximately 95% of the tensile performance of the wrought alloy. Notably, the properties of HW-LMD specimens outperformed other processing methods like casting, binder jetting, EBAM, and WAAM.

The correlation between the grain texture and the direction of stress loading significantly influenced the tensile properties by impacting the activation of sliding systems at micro-plasticity sites. In this study, all specimens were tested perpendicularly to the preferred ⟨001⟩ grain orientation. Consequently, due to the pronounced texture effect, failure occurred more rapidly, resulting in a slight decrease in mechanical perperties in comparison to the wrought alloy. The varying tensile properties of HW-LMD specimens along different directions were associated with the direction of stress loading. In specimens machined perpendicularly to the deposition direction, the tensile stress mainly applied to the overlapping areas between different layers and tracks, where metallurgical bonding was weakened. Hence, the tensile properties of HW-LMD Inconel 625 specimens perpendicular to the deposition direction were slightly lower than those of specimens machined parallel to the deposition direction. Similarly, CIPRIANO FARIAS et al [59] observed the anisotropy in the mechanical properties of arc-based DED Inconel 718 in both vertical and horizontal orientations. They provided a comprehensive explanation for this anisotropy in tensile properties through the relationships among grain growth direction, texture characteristics, and stress loading direction.

The differences in the tensile performance of Inconel 625 alloy produced by different manufacturing methods may be attributed to variations in microstructure characteristics. As shown in Fig. 7, for the HW-LMD process adopted in this study, the energy input applied to the feedstock per unit volume was higher than that of conventional LAM methods such as SLM and LMD. Therefore, HW-LMD Inconel 625 specimens possessed larger grain size and primary dendrite spacing, resulting in relatively low tensile properties compared to LMD specimens. However, in comparison to the WAAM process, Inconel 625 specimens manufactured through HW-LMD exhibited a more refined grain structure and homogeneous distribution of elements, rendering the material less susceptible to loading stress. As a result, the HW-LMD Inconel 625 specimens in this study presented higher tensile strength than components fabricated using WAAM technologies.

The fracture morphologies of the HW-LMD Inconel 625 tensile specimens examined by SEM were presented in Fig. 16. The macroscopic appearances of the fractures, as depicted in Figs. 16(a, d), revealed significant fiber zones (I) and smaller shear zones (II) with a limited number of cracks and voids, without any observable defects such as incomplete fusion or slag. During the tensile testing, dislocation accumulation at grain/phase boundaries induced the initiation and propagation of micro-cracks in areas of stress concentration. Consequently, as seen in Figs. 16(b, e), numerous dimples were observed in the fiber zones, indicating that fracture in all tensile specimens can be

characterized as ductile fracture [48]. Furthermore, as a result of the directional growth of columnar dendrites, the fracture surfaces exhibited torn belts in the magnified SEM images displayed in Figs. 16(c, f), suggesting that crack growth was primarily governed by the crystal slip base mechanism.

Figure 17 presented cross-section morphologies of the HW-LMD Inconel 625 tensile fracture in different directions. Similar to the observations in Figs. 16(a, d), the fracture surface profiles of all the tensile specimens exhibited two distinct regions. As shown in Figs. 17(a, c), the central region is relatively flat and perpendicular to the direction of tensile stress, while the outer shear region is inclined at a 45° angle to the axial loading, indicating the

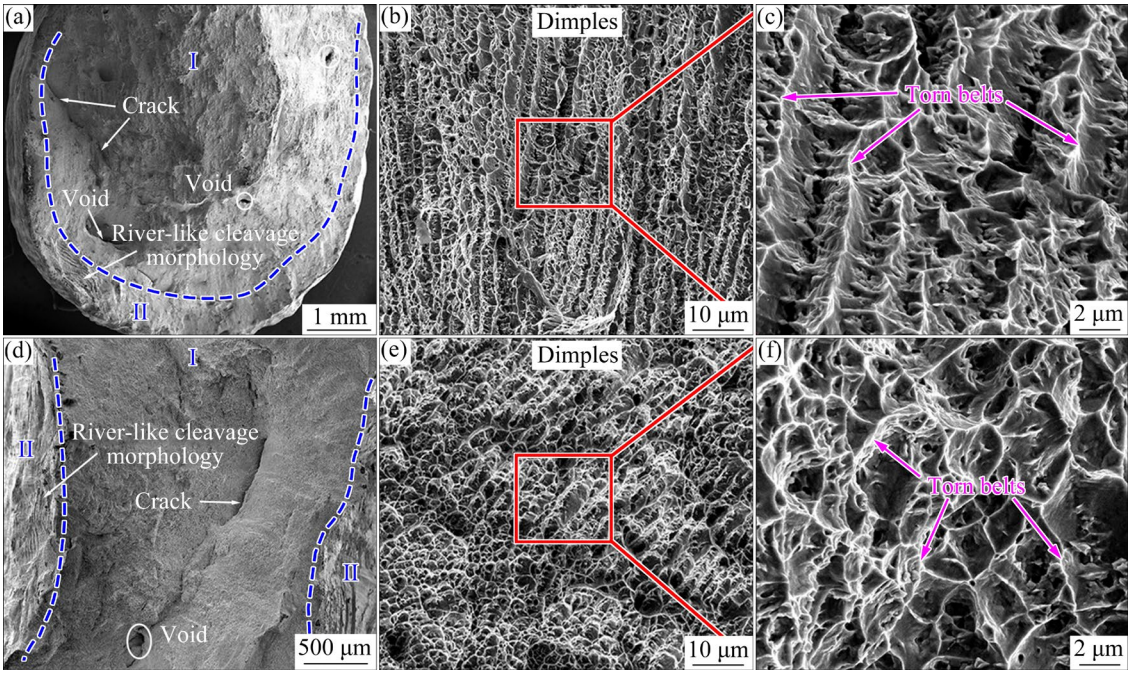

Fig. 16 Fracture morphologies of HW-LMD Inconel 625 tensile specimens: (a−c) In *x* direction; (d−f) In *y* direction

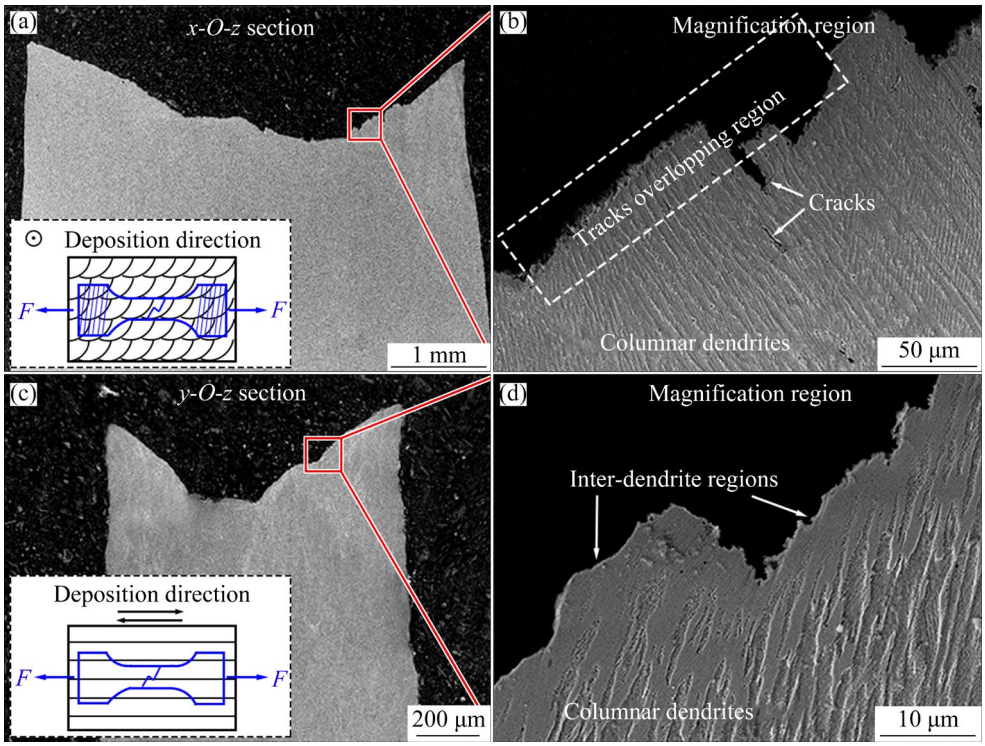

Fig. 17 Cross-section morphologies of HW-LMD Inconel 625 tensile fracture: (a, b) In *x* direction; (c, d) In *y* direction

favorable ductility of the HW-LMD Inconel 625 alloy. The microstructural characteristics in the fracture section can further elucidate the fracture mechanism of the tensile specimens. As mentioned earlier, the microstructure of the HW-LMD Inconel 625 specimens primarily comprises dense columnar dendrites, with the observation of element segregation and brittle Laves phase in the inter-dendritic regions. Therefore, cracks preferentially initiated and propagated at the grain boundaries. The difference between fractures in different directions lay in the locations where the fracture occurred. As seen in Fig. 17(a), when the tensile stress was applied perpendicularly to the deposition direction, it had to cut through several deposited tracks. Consequently, as shown in Fig. 17(b), the fracture typically occurred at the boundaries between different deposited tracks, which generally constitute a weak metallurgical bonding region. Comparatively, Fig. 17(c) elucidated that when the stress was parallel to the deposition direction, the tensile stress only cut through a single deposited layer. Therefore, as demonstrated in Fig. 17(d), the intergranular fracture occurred.

3.4.3 Impact properties

Some nickel-based alloy components employed in aerospace and polar applications must perform effectively in low-temperature environments. To ensure service reliability and investigate the deformation behavior of HW-LMD Inconel 625 components under such conditions, the impact performance of the as-deposited Inconel 625 specimens was examined at 25 and −78 °C. The oscilloscope impact curves shown in Fig. 18 directly depicted the relationship between the impact load and the deformation of the Inconel 625 specimens during testing. For all Inconel 625 specimens tested at room temperature (25 °C) or low temperature (−78 °C), an increase in the impact load led to a corresponding increase in the deformation of specimens. Upon reaching the yield load (F_{gy}), plastic deformation occurred, and cracks were initiated at the point of maximum load (F_m). Subsequently, cracks propagated steadily, causing a decrease in the impact load. Ultimately, the cracks reached a point of instability, leading to the fracture of the impact specimens. The impact load−displacement curves indicated that cracks propagated steadily, without sudden vertical drops in the impact load within a short period, suggesting a ductile fracture in all impact specimens.

The total energy (W_t) consumed during the impact test, represented by the area enclosed in the impact load−displacement curve, comprises the crack initiation energy (W_i) and the crack propagation energy (W_p) [60]. Among them, W_i occurred when the impact load reached its maximum value, which was considered the basis for crack initiation. W_p reflected the alloy's resistance to crack propagation and was a crucial factor in determining the toughness of the alloy. The main energy characteristic values of the HW-LMD Inconel 625 specimens and wrought alloy in impact testing were listed in Table 3. It revealed that at room temperature, W_t and W_p for the HW-LMD specimens were 223.08 and 127.96 J, respectively. At −78 °C, these values decreased to 200.24 and 110.68 J. Notably, the impact toughness of the HW-LMD specimens exceeded 95% that of the wrought alloy, demonstrating superior performance under both room temperature and low-temperature conditions.

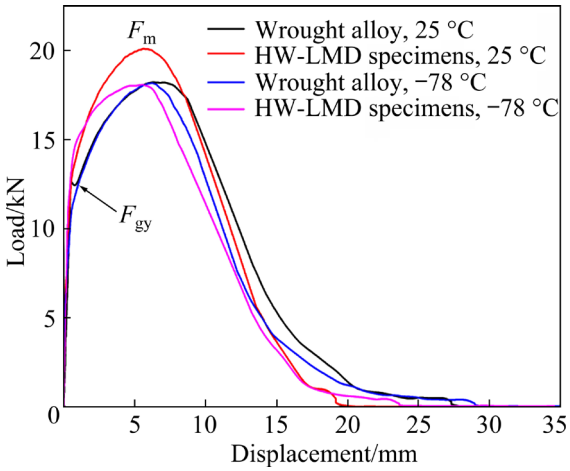

Fig. 18 Load−displacement plots of Inconel 625 specimens during impact tests

Table 3 Results of impact tests for Inconel 625 specimens

Sample	Temperature/°C	W_t/J	W_i/J	W_p/J
Wrought alloy	25	229.56	96.62	132.94
	−78	210.52	94.55	115.97
HW-LMD	25	223.08	95.12	127.96
	−78	200.24	89.56	110.68

Figure 19 presented the surface morphologies of the impact fracture. Similar to the fracture observed in tensile testing, the impact fracture surfaces exhibited extensive fibrous regions at the

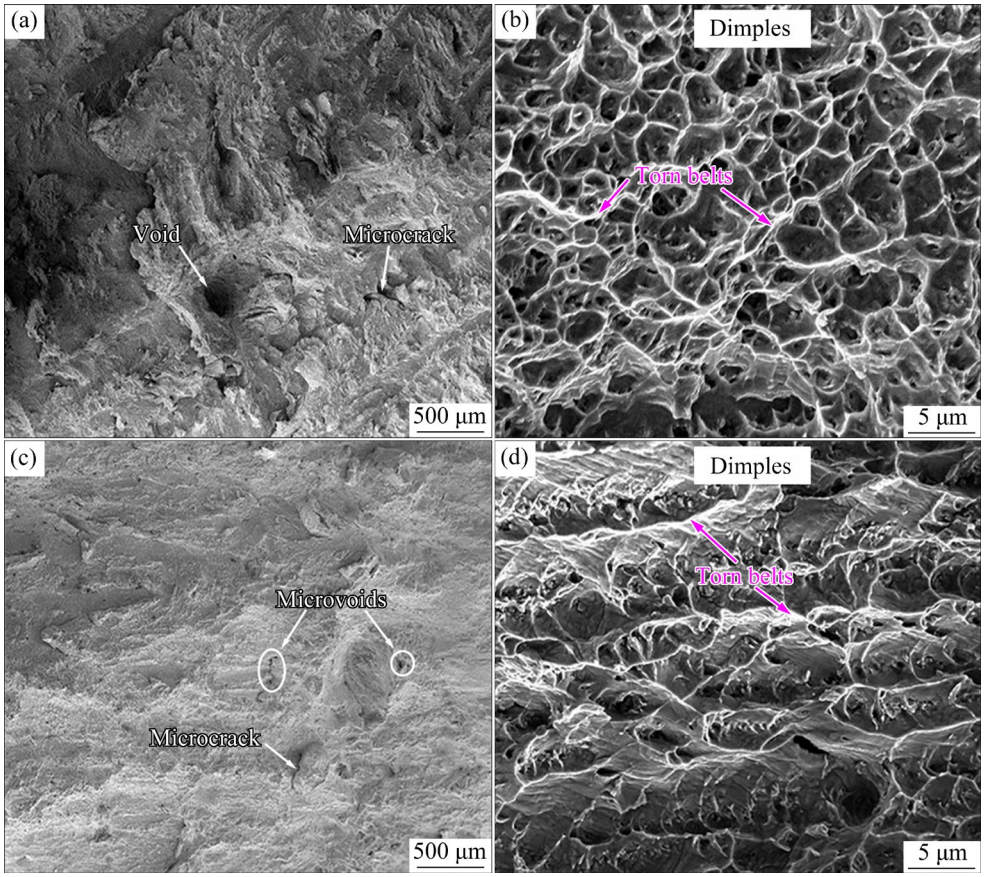

Fig. 19 Impact fracture morphologies of Inconel 625 specimens: (a, b) At room temperature; (c, d) At −78 °C

macroscopic level (see Figs. 19(a, c)), while at the microscopic level, numerous dimples with clusters of torn belts were observed (see Figs. 19(b, d)), indicating a ductile fracture. However, differences in dimple morphology were observed between the fracture surfaces at room temperature and low temperature. As shown in Fig. 19(c), the fracture surface at room temperature featured uniformly distributed and relatively deep dimples, whereas the dimples on the fracture surface at −78 °C (Fig. 19(d)) were relatively shallow. This discrepancy corresponded with the lower impact absorption energies obtained during low-temperature impact testing, as presented in Table 3. The decline in impact properties at low temperatures can be attributed to the reason that atoms were bound so tightly that the movement of the molecules slowed down under the lower temperature, which inhibited the material's ability to withstand impact loading. Consequently, reduced impact absorption energy and corresponding relatively shallow dimples on the fracture surface were observed during impact testing at lower temperatures.

Figure 20 illustrated the typical fracture morphologies of cross-sections of HW-LMD Inconel 625 impact specimens. In the low-magnification SEM images shown in Figs. 20(a, c), the boundaries between adjacent deposited tracks and layers were visible. In the locally magnified region of the transverse section (*x*-*O*-*z* section) depicted in Fig. 20(b), columnar dendrites were evident. The cross-section of the columnar crystals displayed an equiaxed morphology in the horizontal section (*x*-*O*-*y* section), as presented in Fig. 20(d). Furthermore, as observed in Fig. 20(b), the contour line of the fracture was nearly parallel to the growth direction of the columnar crystals. Therefore, it can be inferred that the fracture during the impact tests also occurred at the grain boundaries.

4 Conclusions

(1) The microstructure of the HW-LMD Inconel 625 specimens mainly consisted of columnar dendrites, with an average grain size of 12.5 μm. The growth orientations of the columnar dendrites in different regions were related to the heat dissipation direction. EBSD testing revealed a prominent texture

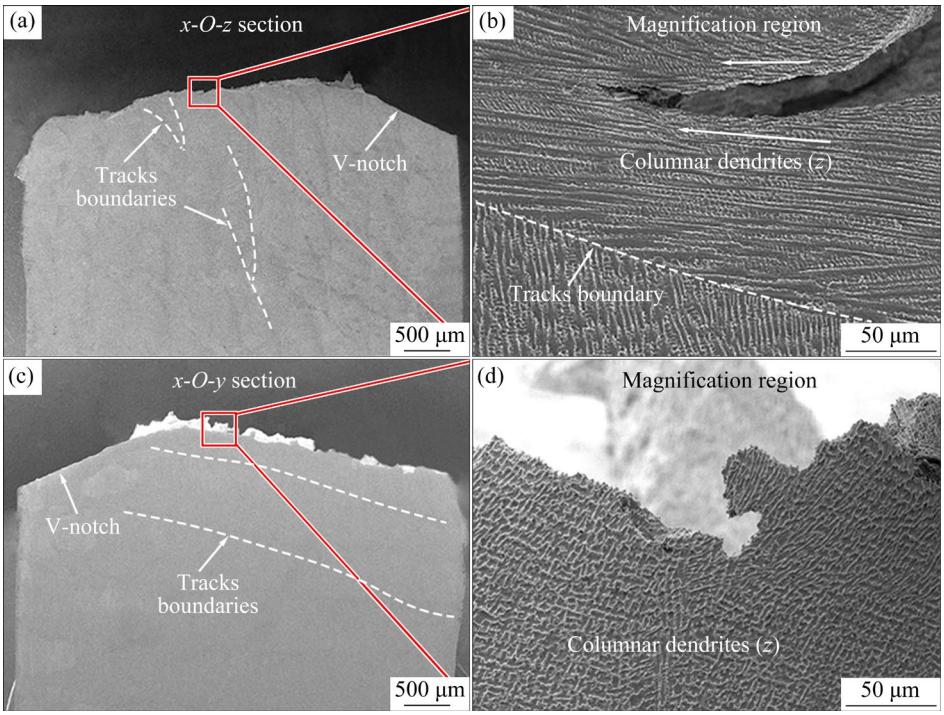

Fig. 20 Typical fracture morphologies of cross-sections of HW-LMD Inconel 625 impact specimens: (a, b) *x*-*O*-*z* section; (c, d) *x*-*O*-*y* section

of {100}⟨001⟩ in columnar dendrites. *γ*-Ni (FCC) was the main phase presented in the HW-LMD Inconel 625 specimens, with the observation of Laves phase and carbides within the inter-dendritic regions. Due to the high cooling rate in the HW-LMD process, elemental segregation and precipitation of large-sized Laves phases were effectively suppressed.

(2) The microhardness of the HW-LMD Inconel 625 specimens from top layer to bottom layer varied from $HV_{1.0}$ 250 to $HV_{1.0}$ 265, of which the average value was 35.7% higher than that of wrought alloy. Along the deposition direction, the ultimate tensile strength (σ_b) and yield strength ($\sigma_{0.2}$) of HW-LMD Inconel 625 specimens were 837.4 and 493.5 MPa, respectively. Perpendicular to the deposition direction, the values were 822.6 and 486.7 MPa, respectively. The tensile strength of the HW-LMD specimens reached up to 95% that of the wrought alloy, demonstrating superiority over traditional WAAM techniques. The impact absorbing energies of the HW-LMD Inconel 625 specimens were 223.08 J at room temperature and 200.24 J at −78 °C, which were close to the levels of wrought alloy. Both the tensile and impact fractures were identified as ductile fracture due to the presence of large areas of dimples on the fracture surfaces.

CRediT authorship contribution statement

Guo-xing SU: Resources, Conceptualization, Data curation, Investigation, Methodology; **Yu SHI:** Funding acquisition, Project administration, Formal analysis; **Chun-kai LI:** Conceptualization, Formal analysis; **Guang LI:** Formal analysis, Writing − Review & editing; **Gang ZHANG:** Writing − Review & editing.

Declaration of competing interest

The authors declare that they have no known competing financial interests or personal relationships that could have appeared to influence the work reported in this paper.

Acknowledgments

This research was supported by the Special Project of Gansu Province, China (Nos. 23ZDGA010, 22ZD6GA008), the Central Guiding Fund for Local Science and Technology Development Project, China (Nos. 24ZYQA054, 23ZYQA308), and the Key Project of Research and Innovation in Universities, China (No. 2024CXPT-06).

References

[1] YANG F, HOU J S, WANG C S, ZHOU L Z. Effects of solution treatment on microstructure and tensile properties of as-cast alloy 625 [J]. Transactions of Nonferrous Metals

Society of China, 2021, 31: 426−437.

[2] FARIAS F W C, DUARTE V R, FELICE I O, FILHO J D C P, SCHELL N, MAAWAD E, AVILA J A, LI J Y, ZHANG Y, SANTOS T G, OLIVEIRA J P. In situ interlayer hot forging arc-based directed energy deposition of Inconel® 625: Process development and microstructure effects [J]. Additive Manufacturing, 2023, 66: 103476.

[3] RODRIGUES T A, CIPRIANO FARIAS F W, AVILA J A, MAAWAD E, SCHELL N, SANTOS T G, OLIVEIRA J P. Effect of heat treatments on Inconel 625 fabricated by wire and arc additive manufacturing: An in situ synchrotron X-ray diffraction analysis [J]. Science and Technology of Welding and Joining, 2023, 28: 534−539.

[4] KHANNA N, RAVAL P, PATEL D, PRAJAPATI R, SCHOOP J, GAJRANI K K. Assessment of additive and subtractive sustainable manufacturing of Inconel 625 [J]. Tribology International, 2023, 186: 108655.

[5] CHEN Y, ZHANG K, HUANG J, HOSSEINI S R E, LI Z G. Characterization of heat affected zone liquation cracking in laser additive manufacturing of Inconel 718 [J]. Materials & Design, 2016, 90: 586−594.

[6] WANG K M, LIU W, DU D, CHANG B H, LIU G, HU Y L, TONG Y G, ZHANG M J, ZHANG J, JU J. Microstructure and properties of K648 superalloy additively manufactured by extreme high-speed laser metal deposition [J]. Transactions of Nonferrous Metals Society of China, 2024, 34: 2192−2203.

[7] TEBIANIAN M, AGHAIE S, RAZAVI JAFARI N S, ELMI HOSSEINI S R, PEREIRA A B, FERNANDES F A O, FARBAKHTI M, CHEN C, HUO Y M. A review of the metal additive manufacturing processes [J]. Materials, 2023, 16: 7514.

[8] KIM S H, LEE H, YEON S M, ARANAS C, CHOI K, YOON J, YANG S W, LEE H. Selective compositional range exclusion via directed energy deposition to produce a defect-free Inconel 718/SS 316L functionally graded material [J]. Additive Manufacturing, 2021, 47: 102288.

[9] ZHOU S W, XU T Y, HU C, WU H, LIU H L, MA X Q. Effect of different topologies on microstructure and mechanical properties of multilayer coatings deposited by laser cladding with Inconel 625 wire [J]. Surface and Coatings Technology, 2021, 421: 127299.

[10] HUANG W H, CHEN S J, XIAO J, JIANG X Q, JIA Y Z. Laser wire-feed metal additive manufacturing of the Al alloy [J]. Optics & Laser Technology, 2021, 134: 106627.

[11] NI M, CHEN C, XU R F, HOSSEINI S R E, LI R D, ZHANG X Y, ZHOU K C. Microstructure and mechanical properties of additive manufactured Inconel 718 alloy strengthened by oxide dispersion with 0.3 wt.% Sc addition [J]. Journal of Alloys and Compounds, 2022, 918: 165763.

[12] SUI S, LI Z, ZHONG C L, ZHANG Q, GASSER A, CHEN J, CHEW Y, BI G J. Laves phase tuning for enhancing high temperature mechanical property improvement in laser directed energy deposited Inconel 718 [J]. Composites (Part B): Engineering, 2021, 215: 108819.

[13] WANG X C, CHEN C J, QIN L L, ZHANG M. Microstructure evolution and mechanical behavior of Inconel 625 produced using direct laser metal deposition [J]. Physics of Metals and Metallography, 2021, 122: 896−907.

[14] KONG Y, HUANG H H. Effect of intrinsic heat treatment on microstructure and hardness of additively manufactured Inconel 625 alloy by directed energy deposition [J]. Materials & Design, 2022, 224: 111279.

[15] HU Y L, LIN X, LI Y L, ZHANG S Y, ZHANG Q, CHEN W M, LI W, HUANG W D. Influence of heat treatments on the microstructure and mechanical properties of Inconel 625 fabricated by directed energy deposition [J]. Materials Science and Engineering: A, 2021, 817: 141309.

[16] ZHANG Q X, CHEN R, JIN D, ZHOU C, LI X W. The effects of different post-heat treatments on rolling contact fatigue behaviors of direct laser cladding Inconel 625 coatings [J]. Journal of Renewable Materials, 2021, 9: 129−144.

[17] KIM K S, KANG T H, KASSNER M E, SON K T, LEE K A. High-temperature tensile and high cycle fatigue properties of Inconel 625 alloy manufactured by laser powder bed fusion [J]. Additive Manufacturing, 2020, 35: 101377.

[18] ZHOU L, MA G Z, ZHAO H C, MOU H L, XU J F, WANG W Z, XING Z G, LI Y, GUO W L, WANG H D. Research status and prospect of extreme high-speed laser cladding technology [J]. Optics & Laser Technology, 2024, 168: 109800.

[19] HERZOG D, BARTSCH K, BOSSEN B. Productivity optimization of laser powder bed fusion by hot isostatic pressing [J]. Additive Manufacturing, 2020, 36: 101494.

[20] TRIPATHY M, GASKELL K, LAURETO J, DAVAMI K, BEHESHTI A. Elevated temperature fretting wear study of additively manufactured Inconel 625 superalloy [J]. Additive Manufacturing, 2023, 67: 103492.

[21] WANG Q, SHI Y J, LI X F, WANG X G, FAN K J, SUN R. Additive technology of high-frequency induction-assisted laser wire deposition [J]. Optics & Laser Technology, 2023, 167: 109785.

[22] CHEN Y, LU F G, ZHANG K, NIE P L, ELMI HOSSEINI S R, FENG K, LI Z G. Laser powder deposition of carbon nanotube reinforced nickel-based superalloy Inconel 718 [J]. Carbon, 2016, 107: 361−370.

[23] CHEN Y, LU F G, ZHANG K, NIE P L, ELMI HOSSEINI S R, FENG K, LI Z G. Dendritic microstructure and hot cracking of laser additive manufactured Inconel 718 under improved base cooling [J]. Journal of Alloys and Compounds, 2016, 670: 312−321.

[24] ABRANOVIC B, SARKAR S, CHANG-DAVIDSON E, BEUTH J. Melt pool level flaw detection in laser hot wire directed energy deposition using a convolutional long short-term memory autoencoder [J]. Additive Manufacturing, 2024, 79: 103843.

[25] RAHMANI DEHAGHANI M, SAHRAEIDOLATKHANEH A, NILSEN M, SIKSTRÖM F, SAJADI P, TANG Y F, WANG G G. System identification and closed-loop control of laser hot-wire directed energy deposition using the parameter-signature-quality modeling scheme [J]. Journal of Manufacturing Processes, 2024, 112: 1−13.

[26] ZHAO S B, XU S, HUANG Y M, YANG L J. Laser hot-wire cladding of Ni/WC composite coatings with a tubular cored wire [J]. Journal of Materials Processing Technology, 2021, 298: 117273.

[27] NOWOTNY S, BRUECKNER F, THIEME S, LEYENS C, BEYER E. High-performance laser cladding with combined energy sources [J]. Journal of Laser Applications, 2015,

27(Suppl. 1): S17001.

[28] PAJUKOSKI H, NÄKKI J, THIEME S, TUOMINEN J, NOWOTNY S, VUORISTO P. High performance corrosion resistant coatings by novel coaxial cold- and hot-wire laser cladding methods [J]. Journal of Laser Applications, 2016, 28: 012011.

[29] ZHANG Z, KONG F R, KOVACEVIC R. Laser hot-wire cladding of Co−Cr−W metal cored wire [J]. Optics and Lasers in Engineering, 2020, 128: 105998.

[30] ABIOYE T E, FOLKES J, CLARE A T. A parametric study of Inconel 625 wire laser deposition [J]. Journal of Materials Processing Technology, 2013, 213: 2145−2151.

[31] WEI S P, WANG G, SHIN Y C, RONG Y M. Comprehensive modeling of transport phenomena in laser hot-wire deposition process [J]. International Journal of Heat and Mass Transfer, 2018, 125: 1356−1368.

[32] HUANG W H, XIAO J, CHEN S J, JIANG X Q. Control of wire melting behavior during laser hot wire deposition of aluminum alloy [J]. Optics & Laser Technology, 2022, 150: 107978.

[33] NGUEJIO J, SZMYTKA F, HALLAIS S, TANGUY A, NARDONE S, GODINO MARTINEZ M G. Comparison of microstructure features and mechanical properties for additive manufactured and wrought nickel alloys 625 [J]. Materials Science and Engineering: A, 2019, 764: 138214.

[34] MARCHESE G, LORUSSO M, PARIZIA S, BASSINI E, LEE J W, CALIGNANO F, MANFREDI D, TERNER M, HONG H U, UGUES D, LOMBARDI M, BIAMINO S. Influence of heat treatments on microstructure evolution and mechanical properties of Inconel 625 processed by laser powder bed fusion [J]. Materials Science and Engineering: A, 2018, 729: 64−75.

[35] WANG P, ZHANG B C, TAN C C, RAGHAVAN S, LIM Y F, SUN C N, WEI J, CHI D Z. Microstructural characteristics and mechanical properties of carbon nanotube reinforced Inconel 625 parts fabricated by selective laser melting [J]. Materials & Design, 2016, 112: 290−299.

[36] ROMBOUTS M, MAES G, MERTENS M, HENDRIX W. Laser metal deposition of Inconel 625: Microstructure and mechanical properties [J]. Journal of Laser Applications, 2012, 24: 052007.

[37] HAO J B, HU F T, LE X W, LIU H, YANG H F, HAN J. Microstructure and high-temperature wear behaviour of Inconel 625 multi-layer cladding prepared on H13 mould steel by a hybrid additive manufacturing method [J]. Journal of Materials Processing Technology, 2021, 291: 117036.

[38] WANG J F, SUN Q J, WANG H, LIU J P, FENG J C. Effect of location on microstructure and mechanical properties of additive layer manufactured Inconel 625 using gas tungsten arc welding [J]. Materials Science and Engineering: A, 2016, 676: 395−405.

[39] SILWAL B, WALKER J, WEST D. Hot-wire GTAW cladding: Inconel 625 on 347 stainless steel [J]. The International Journal of Advanced Manufacturing Technology, 2019, 102: 3839−3848.

[40] WANG Y F, CHEN X Z, SU C C. Microstructure and mechanical properties of Inconel 625 fabricated by wire-arc additive manufacturing [J]. Surface and Coatings Technology, 2019, 374: 116−123.

[41] RAVI G, MURUGAN N, ARULMANI R. Microstructure and mechanical properties of Inconel-625 slab component fabricated by wire arc additive manufacturing [J]. Materials Science and Technology, 2020, 36: 1785−1795.

[42] CHEN L, SUN Y Z, LI L, REN X D. Microstructure evolution, mechanical properties, and strengthening mechanism of TiC reinforced Inconel 625 nanocomposites fabricated by selective laser melting [J]. Materials Science and Engineering: A, 2020, 792: 139655.

[43] CHEN Y, LU F G, ZHANG K, NIE P L, ELMI HOSSEINI S R, FENG K, LI Z G, CHU P K. Investigation of dendritic growth and liquation cracking in laser melting deposited Inconel 718 at different laser input angles [J]. Materials & Design, 2016, 105: 133−141.

[44] ABIOYE T E, MCCARTNEY D G, CLARE A T. Laser cladding of Inconel 625 wire for corrosion protection [J]. Journal of Materials Processing Technology, 2015, 217: 232−240.

[45] WANG Q Y, PEI R, LIU S, WANG S L, DONG L J, ZHOU L J, XI Y C, BAI S L. Microstructure and corrosion behavior of different clad zones in multi-track Ni-based laser-clad coating [J]. Surface and Coatings Technology, 2020, 402: 126310.

[46] MOHAMMADPOUR P, YUAN H, PHILLION A B. Microstructure evolution of Inconel 625 alloy during single-track laser powder bed fusion [J]. Additive Manufacturing, 2022, 55: 102824.

[47] MENG G R, GONG Y D, ZHANG J D, JIANG Z Z, REN Q Z, ZHAO J B. Microstructure and mechanical properties of Inconel 718 thin walls prepared by laser direct energy deposition and selective laser melting [J]. Thin-Walled Structures, 2023, 193: 111284.

[48] SAFARZADE A, SHARIFITABAR M, SHAFIEE AFARANI M. Effects of heat treatment on microstructure and mechanical properties of Inconel 625 alloy fabricated by wire arc additive manufacturing process [J]. Transactions of Nonferrous Metals Society of China, 2020, 30: 3016−3030.

[49] LUO K Y, LI S H, XU G, HOSSEINI S R E, LU J Z. Hot corrosion behaviors of directed energy deposited Inconel 718/Haynes 25 functionally graded material at 700 °C and 900 °C [J]. Corrosion Science, 2022, 197: 110040.

[50] KELLER T, LINDWALL G, GHOSH S, MA L, LANE B M, ZHANG F, KATTNER U R, LASS E A, HEIGEL J C, IDELL Y, WILLIAMS M E, ALLEN A J, GUYER J E, LEVINE L E. Application of finite element, phase-field, and CALPHAD-based methods to additive manufacturing of Ni-based superalloys [J]. Acta Materialia, 2017, 139: 244−253.

[51] GAO J, MA Q C, SUN Y, WANG K N, SONG Q, WANG C M. Effect of Nb content on microstructure and corrosion resistance of Inconel 625 coating formed by laser cladding [J]. Surface and Coatings Technology, 2023, 458: 129311.

[52] GU D D, ZHANG H M, DAI D H, XIA M J, HONG C, POPRAWE R. Laser additive manufacturing of nano-TiC reinforced Ni-based nanocomposites with tailored microstructure and performance [J]. Composites (Part B): Engineering, 2019, 163: 585−597.

[53] SUI S, CHEN J, MA L, FAN W, TAN H, LIU F C, LIN X. Microstructures and stress rupture properties of pulse laser repaired Inconel 718 superalloy after different heat treatments

[J]. Journal of Alloys and Compounds, 2019, 770: 125−135.
[54] WU B, LIANG J J, ZHOU Y Z, YANG Y H, LI J G, SUN X F. Influence of laser power on microstructure and tensile property of a new nickel-based superalloy designed for additive manufacturing [J]. Transactions of Nonferrous Metals Society of China, 2023, 33: 1124−1143.
[55] LI W Q, SUGIO K, LIU X G, YAMAMOTO M, GUO Y, ZHU S, SASAKI G. Microstructure evolution and mechanical properties of 308L stainless steel coatings fabricated by laser hot wire cladding [J]. Materials Science and Engineering: A, 2021, 824: 141825.
[56] XU F J, LV Y H, LIU Y X, SHU F Y, HE P, XU B S. Microstructural evolution and mechanical properties of Inconel 625 alloy during pulsed plasma arc deposition process [J]. Journal of Materials Science & Technology, 2013, 29: 480−488.
[57] GONZALEZ J A, MIRELES J, STAFFORD S W, PEREZ M A, TERRAZAS C A, WICKER R B. Characterization of Inconel 625 fabricated using powder-bed-based additive manufacturing technologies [J]. Journal of Materials Processing Technology, 2019, 264: 200−210.
[58] MURR L E, MARTINEZ E, GAYTAN S M, RAMIREZ D A, MACHADO B I, SHINDO P W, MARTINEZ J L, MEDINA F, WOOTEN J, CISCEL D, ACKELID U, WICKER R B. Microstructural architecture, microstructures, and mechanical properties for a nickel-base superalloy fabricated by electron beam melting [J]. Metallurgical and Materials Transactions A, 2011, 42: 3491−3508.
[59] CIPRIANO FARIAS F W, REBELO DUARTE V, DA CRUZ PAYÃO FILHO J, SCHELL N, MAAWAD E, BORDAS-CZAPLICKI M, ALVES DA FONSECA F M, CORMIER J, GOMES DOS SANTOS T J, OLIVEIRA J P. Arc-based directed energy deposited Inconel 718: Role of heat treatments on high-temperature tensile behavior [J]. Materials Research Letters, 2024, 12: 97−107.
[60] PUPPALA G, MOITRA A, SATHYANARAYANAN S, KAUL R, SASIKALA G, PRASAD R C, KUKREJA L M. Evaluation of fracture toughness and impact toughness of laser rapid manufactured Inconel-625 structures and their co-relation [J]. Materials & Design, 2014, 59: 509−515.

激光热丝金属沉积增材制造 Inconel 625 合金的工艺、显微组织与力学性能

苏国兴，石 玗，李春凯，李 广，张 刚

兰州理工大学 省部共建有色金属先进加工与再利用全国重点实验室，兰州 730050

摘 要：采用激光热丝沉积技术(HW-LMD)，通过过程优化制备了 Inconel 625 合金构件，焊丝沉积速率达到 1.72 kg/h。系统研究了 HW-LMD Inconel 625 合金的显微组织和力学性能。结果表明，HW-LMD Inconel 625 合金的显微组织由柱状树枝晶构成，其平均晶粒尺寸为 12.5 μm，合金中存在强{100}⟨001⟩织构。合金的主要相为 γ-Ni，且在柱状树枝晶晶间区域存在尺寸小于 1 μm 的 Laves 相。合金的平均硬度为 $HV_{1.0}$ 258，屈服强度和极限抗拉强度分别为 493.5 和 837.4 MPa，断后伸长率超过 50%。合金在 25 和−78 ℃下的冲击吸收功分别为 223.08 和 200.24 J。合金的拉伸和冲击断口表面均呈韧窝特征，表明合金在变形过程中发生了韧性断裂。

关键词：激光金属沉积；热丝；Inconel 625 合金；显微组织；力学性能

(Edited by Wei-ping CHEN)